

DualSwinFusionSeg: Multimodal Martian Landslide Segmentation via Dual Swin Transformer with Multi-Scale Fusion and UNet++

Shahriar Kabir^{1,*}, Abdullah Muhammed Amimul Ehsan^{1,*}, Istiak Ahmmed Rifti^{1,*},
Md Kaykobad Reza²

¹Bangladesh University of Engineering and Technology, Bangladesh

²University of California, Riverside, USA

kabirshahriar468@gmail.com amimul.ehsan2001@gmail.com

riftirc96@gmail.com mreza025@ucr.edu

*Equal contribution

Abstract

*Automated segmentation of Martian landslides, particularly in tectonically active regions such as Valles Marineris, is important for planetary geology, hazard assessment, and future robotic exploration. However, detecting landslides from planetary imagery is challenging due to the heterogeneous nature of available sensing modalities and the limited number of labeled samples. Each observation combines RGB imagery with geophysical measurements such as digital elevation models, slope maps, thermal inertia, and contextual grayscale imagery, which differ significantly in resolution and statistical properties. To address these challenges, we propose **DualSwinFusionSeg**, a multimodal segmentation architecture that separates modality-specific feature extraction and performs multi-scale cross-modal fusion. The model employs two parallel Swin Transformer V2 encoders to independently process RGB and auxiliary geophysical inputs, producing hierarchical feature representations. Corresponding features from the two streams are fused at multiple scales and decoded using a UNet++ decoder with dense nested skip connections to preserve fine boundary details. Extensive ablation studies evaluate modality contributions, loss functions, decoder architectures, and fusion strategies. Experiments on the MMLSv2 dataset from the PBVS 2026 Mars-LS Challenge show that modality-specific encoders and simple concatenation-based fusion improve segmentation accuracy under limited training data. The final model achieves 0.867 mIoU and 0.905 F1 on the development benchmark and 0.783 mIoU on the held-out test set, demonstrating strong performance for multimodal planetary surface segmentation.*

1. Introduction

Landslides are among the most significant mass-wasting processes shaping the surfaces of rocky planetary bodies. On Mars, they modify crater walls, polar scarps, and volcanic flanks, providing valuable geomorphological evidence of subsurface volatiles and potential past liquid activity. Accurate mapping of these features is important for planetary geology, hazard assessment, and future robotic exploration. However, manual annotation of landslides from orbital imagery is time-consuming and difficult to scale to planetary-level analysis. Automated segmentation methods offer a practical solution but remain challenging due to severe class imbalance, large morphological variability across terrains, and the heterogeneous nature of multi-sensor observations.

The PBVS 2026 Martian Landslide Segmentation (MARS-LS) Challenge addresses this problem using a multimodal remote sensing dataset designed for binary landslide segmentation. Each 128×128 GeoTIFF tile contains seven co-registered channels, including three RGB bands and four geophysical modalities: Digital Elevation Model (DEM), slope, THEMIS thermal inertia, and CTX grayscale context imagery. These modalities span dramatically different spatial resolutions, ranging from approximately 6 m for CTX grayscale imagery to approximately 232 m for the Viking RGB mosaic. Furthermore, only 531 labeled tiles are available for training and validation, placing the problem firmly in a small-data regime where effective multimodal feature representation and robust architectural design are critical.

To address these challenges, we propose **DualSwinFusionSeg**, a multimodal segmentation framework that explicitly separates modality-specific feature extraction while enabling efficient cross-modal interaction. The model employs two parallel Swin Transformer V2-Small encoders that independently process RGB imagery and auxiliary geophysical inputs, producing hierarchical feature representations. Fea-

tures from the two streams are fused at multiple pyramid levels using lightweight concatenation-projection modules and decoded using a UNet++ architecture with dense nested skip connections to preserve fine spatial details. To better understand design trade-offs under limited data, we conduct extensive ablation studies covering modality combinations, loss functions, decoder architectures, fusion strategies, attention modules, hybrid decoding designs, test-time augmentation, and exponential moving average training.

The main contributions of this work are:

- A **dual-encoder multimodal architecture** that processes RGB and geophysical inputs using Swin Transformer V2 encoders and performs multi-scale feature fusion through lightweight concatenation-projection modules.
- A **decoder-agnostic** multimodal segmentation framework with test-time augmentation, where the main proposed model uses a UNet++ decoder and achieves the best mIoU, while a hybrid SegFormer–UNet++ decoder is evaluated separately in ablation.
- A comprehensive **multi-axis ablation study**, providing insights into effective architectural choices for multimodal segmentation under small labeled training data constraints.

Our model achieves **0.867 mIoU (F1 = 0.905)** on the development benchmark and **0.783 mIoU (F1 = 0.800)** on the held-out test phase of the PBVS 2026 MARS-LS Challenge.

2. Related Work

Semantic Segmentation Architectures has evolved from early fully convolutional networks [12], which enabled pixel-wise prediction, to encoder–decoder models that better preserve spatial details through skip connections. Among them, U-Net [18] became influential because of its simple design and effective multiscale feature aggregation. Later methods improved context modeling and boundary refinement. DeepLabv3+ [3] combined atrous spatial pyramid pooling with an encoder–decoder framework for sharper segmentation, while UNet++ [26] redesigned skip connections with nested dense pathways to reduce the semantic gap between encoder and decoder features. More recently, transformer-based models have shown strong results in dense prediction. Architectures such as SegFormer [24] and Swin [11] show that hierarchical transformers can capture long-range context while preserving multiscale structure. Together, these advances motivate the use of transformer encoders with multiscale decoders for challenging segmentation tasks.

Landslide Segmentation in Remote Sensing remains difficult because of large intra-class variability, complex terrain, and limited annotated data. The Landslide4Sense benchmark [4] introduced a standardized multimodal dataset and showed that combining optical imagery with terrain features such as DEM and slope improves performance. Building on this, recent studies have explored stronger multimodal

fusion and better representation learning. For example, AST-UNet [9] enhances SwinUNet with attention mechanisms to improve boundary continuity and reduce noise. D2FLS-Net [25] further proposes a dual-stage DEM-guided fusion transformer for more effective integration of terrain and image features. Another direction uses vision foundation models; TransLandSeg [5] adapts a pretrained transformer.

Martian Landslide Segmentation. Compared with terrestrial landslide detection, Martian landslide segmentation from orbital imagery is still relatively underexplored. One of the earliest works, MarsLS-Net [14], introduced both a multimodal architecture and a benchmark dataset for this task. More recently, MMLSv2 [15] expanded this line of work with a seven-band multimodal dataset. These studies show that Martian landslide detection differs from Earth-based settings in two major ways: labeled data are extremely limited, and useful information is spread across heterogeneous modalities such as high-resolution imagery, elevation, and thermal measurements. This makes Mars a strong testbed for architectures that can balance modality-specific representation learning with efficient multimodal fusion.

3. Proposed Method

We introduce DualSwinFusionSeg, a multimodal binary segmentation model for heterogeneous, multi-resolution Mars orbital data. As shown in Figure 1, it comprises: (i) two hierarchical vision transformer encoders extracting scale-wise features from RGB and auxiliary geophysical inputs; (ii) a cross-modal fusion module integrating the features at each scale; and (iii) a dense decoder predicting the segmentation mask. Prediction after feature fusion can be written as:

$$\hat{y} = \sigma(\text{Up}(\text{Head}(\text{UNet}++(\{F^l\}_{l=1}^4)))) \quad (1)$$

where F^l is the fused feature at scale l and $\hat{y} \in [0, 1]^{H \times W}$ is the per-pixel landslide probability.

3.1. Input Representation

Each 128×128 GeoTIFF tile contains seven co-registered channels derived from five instruments across four Mars orbital missions. Rather than treating them as a single tensor, we split them into two semantically coherent groups. The RGB tensor $X^{\text{rgb}} \in \mathbb{R}^{B \times 3 \times H \times W}$ comprises bands 5–7 (red, green, blue) from the Viking colorized global mosaic (~ 232 m/pixel). The auxiliary tensor $X^{\text{aux}} \in \mathbb{R}^{B \times 4 \times H \times W}$ contains THEMIS thermal inertia (band 1), slope (band 2), DEM (band 3), and CTX greyscale imagery (band 4), jointly encoding thermophysical properties, terrain geometry, and medium-resolution optical context (~ 6 – 200 m). Both tensors are resized to a common input size $H \times W$ (default 128×128) and normalized in two steps: per-image, per-band percentile scaling (P_1 – P_{99} to $[0, 1]$), followed by channel-wise standardization using dataset-level mean and standard deviation (Section 4.2).

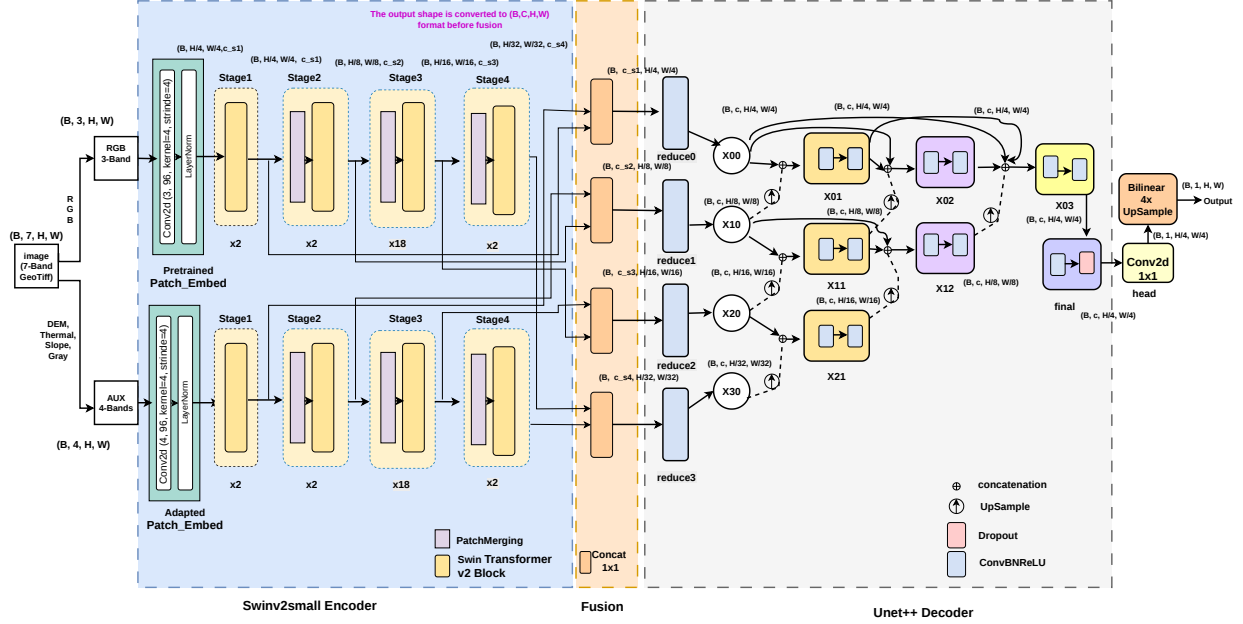


Figure 1. DualSwinFusionSeg: two SwinV2-Small encoders process RGB and AUX inputs into four-level feature hierarchies; per-scale features are concatenated, reduced via 1×1 convolution, and decoded by UNet+, followed by a Conv 1×1 head and bilinear upsampling to the final segmentation mask.

3.2. Dual Swin Encoder

A single encoder struggles to reconcile RGB imagery and DEM/slope fields because their dynamic ranges, spatial frequencies, and pixel semantics differ. We therefore use two *independent* Swin Transformer V2-Small (SwinV2-S) backbones [11], producing separate hierarchical feature representations for each modality before fusion.

Swin Transformer V2 backbone. SwinV2 computes self-attention in non-overlapping 8×8 windows, alternating regular and shifted windows for cross-window interaction. It uses log-spaced continuous position bias (Log-CPB) [11] for relative positional encoding which generalizes better to unseen resolutions than the discrete bias of the original Swin [10]. For 128×128 input, it outputs four stages with strides $\{4, 8, 16, 32\}$, channels $\{96, 192, 384, 768\}$, and map sizes $\{32 \times 32, 16 \times 16, 8 \times 8, 4 \times 4\}$. Both encoders use `features_only=True` and `out_indices=(0, 1, 2, 3)`. Although the checkpoint name is `swinv2_small_window8_256`, we set `patch_embed.img_size=None` and `patch_embed.strict_img_size=False`, enabling 128×128 inputs.

Encoder initialization. Both encoders load ImageNet-21k pretrained weights of `swinv2_small_window8_256` from `timm` [21], each initialized independently from the same checkpoint. For the AUX encoder, the patch-

embedding convolution $W_0 \in \mathbb{R}^{96 \times 3 \times 4 \times 4}$ is replaced by $W' \in \mathbb{R}^{96 \times 4 \times 4 \times 4}$: channels 1–3 copy W_0 directly, and channel 4 is set to the per-position RGB mean, $W'_{:,4,:,:} = \frac{1}{3} \sum_{c=1}^3 W_{0,,:,c,:}$. This *channel-mean warm initialization* preserves pretrained spatial filters for the first three channels while providing a reasonable starting point for the CTX greyscale channel (band 4); all other transformer block weights remain unchanged from the pretrained checkpoint.

3.3. Cross-Modal Feature Fusion

Let $F_{\text{RGB}}^l, F_{\text{aux}}^l \in \mathbb{R}^{B \times C_l \times H_l \times W_l}$ denote the feature maps from the two encoders at pyramid scale $l \in \{1, 2, 3, 4\}$, with $C_l \in \{96, 192, 384, 768\}$. The streams are fused via channel-wise concatenation followed by 1×1 convolution:

$$F^l = f_{\theta}^l([F_{\text{RGB}}^l \parallel F_{\text{aux}}^l]), \quad l = 1, \dots, 4, \quad (2)$$

where f_{θ}^l is a 1×1 convolution that reduces the $2C_l$ -channel tensor back to C_l . Four independent per-scale Conv(1×1)-BN-ReLU projections inside the decoder then map each scale to $C=256$ channels at the decoder input. This design enables per-location channel mixing without spatial token interaction. Compared to cross-attention, it avoids the quadratic attention term $O(N^2 C_l)$ and uses pointwise-convolution compute $O(N C_l^2)$ with $O(C_l^2)$ parameters per scale.

3.4. Decoder Network and Classification Head

The fused feature pyramid $\{F^l\}_{l=1}^4$ is decoded by UNet++ [26], which extends U-Net with *dense nested skip connections* that progressively transform encoder features before fusion. Formally, at node (i, j) :

$$\mathbf{x}^{i,j} = \mathcal{H}_{i,j} \left(\text{Cat} \left(\{\mathbf{x}^{i,k}\}_{k=0}^{j-1}, \text{Up}(\mathbf{x}^{i+1,j-1}) \right) \right), \quad j \geq 1, \quad (3)$$

where $\mathbf{x}^{i,0} = \text{Proj}_i(F^{i+1})$ denotes the projected encoder feature at scale $i \in \{0, 1, 2, 3\}$, $\text{Up}(\cdot)$ is bilinear upsampling, and $\mathcal{H}_{i,j}$ is a block with two Conv(3×3)-BatchNorm-ReLU layers. Deep supervision is disabled in default setting; only the final decoder output node (denoted $\mathbf{x}^{0,3}$) contributes to the loss. Prior to the dense nodes, four independent Conv(1×1)-BN-ReLU projections map each encoder scale $\{96, 192, 384, 768\}$ to a common $C=256$ -channel space. The final node $\mathbf{x}^{0,3}$ is refined by a Conv(3×3)-BN-ReLU followed by Dropout ($p = 0.1$), then a Conv(1×1) head outputs a single logit map, bilinearly upsampled to expected output resolution(128×128).

The network has **~113 M parameters**: two SwinV2-S encoders (49 M each), fusion layers (1.6 M), and the UNet++ decoder (13.9 M).

3.5. Training Objective

We train the network with a composite loss combining class-weighted Binary Cross-Entropy (BCE) and soft Dice:

$$\mathcal{L} = \frac{1}{2} \mathcal{L}_{\text{BCE}}(w^+) + \frac{1}{2} \mathcal{L}_{\text{Dice}}, \quad (4)$$

where $w^+ = N_{\text{neg}}/N_{\text{pos}} \approx 1.86$ compensates for the $\sim 35\%$ foreground ratio, and $\hat{p}_i = \sigma(z_i)$ is the predicted probability. The soft Dice loss is

$$\mathcal{L}_{\text{Dice}} = 1 - \frac{2 \sum_i \hat{p}_i y_i}{\sum_i \hat{p}_i + \sum_i y_i + \varepsilon}, \quad \varepsilon = 10^{-7}. \quad (5)$$

BCE provides stable per-pixel gradients to prevent collapse to background, while Dice directly maximizes intersection-over-union, aligning training with mIoU evaluation. Ablations over ten alternative losses (Section 4.4.2) show this combination consistently outperforms each term alone and other variants including focal, Tversky, soft-IoU, and boundary Dice losses. Table 1 shows choices of hyperparameters during training.

4. Experimental Results

4.1. PBVS 2026 MARS-LS Dataset

The MARS-LS challenge dataset [16] is based on MMLSv2 and provides co-registered 128×128 GeoTIFF tiles with pixel-wise binary landslide masks. Each tile contains seven aligned channels: thermal inertia (band 1; THEMIS, ~ 100 m/pixel), slope (band 2; derived from DEM), DEM

Table 1. Training hyperparameters used across all experiments.

Hyperparameter	Value	Hyperparameter	Value
Optimiser	AdamW	Epochs / fold	50
Learning rate	2×10^{-4}	Batch size	16
Weight decay	10^{-4}	Precision	FP16
LR warm-up	3 epochs	LR schedule	Cosine
EMA decay (γ)	0.995	CV folds	5

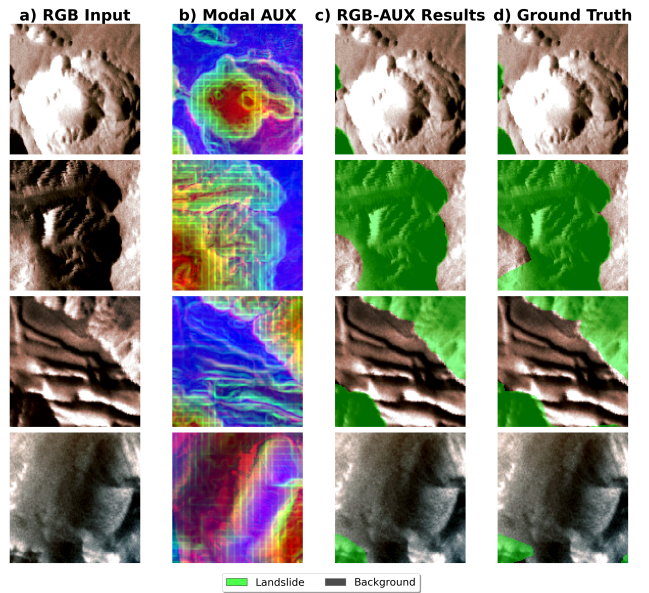


Figure 2. Qualitative segmentation results.

Table 2. Official CodaBench evaluation for the final submission.

Phase	mIoU	IoU _{fg}	IoU _{bg}	F1	Prec.	Recall
Development	0.867	0.827	0.907	0.905	0.900	0.911
Test	0.783	0.677	0.890	0.800	0.760	0.860

(band 3; MOLA blended with HRSC, ~ 200 m/pixel), grayscale imagery (band 4; CTX, ~ 6 m/pixel), and RGB basemap channels (bands 5-7; Viking colored global mosaic, ~ 232 m/pixel). This heterogeneous, multi-source input motivates the dual-encoder design in Section 3.

Dataset splits and class statistics. The official development data comprises 465 labelled training tiles and 66 labelled validation tiles. The positive-class weight, $w^+ = N_{\text{neg}}/N_{\text{pos}} \approx 1.86$, computed from the training tiles, accounts for moderate class imbalance, with foreground pixels averaging $\sim 35.4\%$ across the training set.

Preprocessing. A two-stage normalization pipeline is applied consistently during training and inference to ensure stable input statistics. *Stage 1*: each tile-channel is clipped to its $[P_1, P_{99}]$ percentile range and linearly rescaled to $[0, 1]$, mitigating sensor artifacts and extreme terrain outliers. *Stage 2*:

dataset-level z-score standardization, $x' = (x - \mu_c) / (\sigma_c + \epsilon)$, is applied using channel-wise statistics computed solely from the training tiles.

4.2. Implementation Details

Hardware and software. All experiments were conducted on Kaggle computational notebooks using 4 vCPUs (Intel Xeon @ 2.00 GHz), 31 GiB system RAM, and 2× NVIDIA Tesla T4 GPUs (16 GiB VRAM each; CUDA 13.0). The implementation is based on Python 3.12, PyTorch 2.9+cu126, the `timm` model library [21] for SwinV2 backbone loading, Albumentations [2] for online data augmentation, and `rasterio` for GeoTIFF input/output.

Data augmentation. To mitigate overfitting on the limited training set, online augmentation is applied during training. Geometric transformations are applied jointly to all input channels and the segmentation mask to preserve spatial consistency. Photometric transformations are restricted to RGB, as altering geophysical channels (DEM, Slope, Thermal) would distort their physically meaningful values (Table 4).

Optimisation. All models are trained with the AdamW optimizer [13] under mixed-precision (FP16). A 3-epoch linear learning-rate warm-up is followed by cosine annealing for the remaining epochs. An exponential moving average (EMA) of model weights with decay $\gamma = 0.995$ is maintained throughout training. After each epoch, both instantaneous and EMA weights are evaluated on the held-out fold, and the checkpoint with higher mIoU is retained.

Ensemble inference and test-time augmentation. For inference, the five fold-best checkpoints predictions are combined via ensemble averaging: each test tile is processed by all five models, and the resulting probability maps are averaged pixel-wise. Four-view test-time augmentation (TTA) is applied, processing the original tile and three transformed versions (horizontal flip, vertical flip, 90° rotation) through the ensemble, producing $5 \times 4 = 20$ probability maps per tile. These maps are averaged and thresholded at $\tau = 0.51$ to yield the final binary mask.

4.3. Main Results

Table 2 presents the official metrics from the PBVS 2026 CodaBench evaluation server for the submitted model. The final model achieves $\text{mIoU} = 0.867$ and $\text{F1} = 0.905$ on the development phase, and $\text{mIoU} = 0.783$ and $\text{F1} = 0.800$ on the held-out test phase. The development score notably exceeds the 5-fold cross-validation mean ($\text{mIoU} = 0.84$) primarily because the 20-prediction ensemble (5 folds \times 4 TTA views) combined with EMA weight averaging substantially reduces prediction variance relative to any single fold checkpoint.

The $\Delta\text{mIoU} = 0.084$ gap between development and test phases is consistent with domain shift rather than training-set overfitting. Notably, the precision drop ($0.900 \rightarrow 0.760$) exceeds the recall drop ($0.911 \rightarrow 0.860$), indicating that

the model retains sensitivity to landslide deposits but generates more false positives on geologically similar features in the test domain. Table 3 traces the step-by-step mIoU improvement from the initial baseline to the final submission, demonstrating a consistent progression driven by each architectural and training decision.

Figure 2 shows representative qualitative results, highlighting predicted masks against ground truth.

4.4. Ablation Studies

A systematic ablation study was conducted to isolate the contribution of each design decision. Each ablation varies a single component while holding all others fixed at their best-known settings.

4.4.1. Ablation study on modality combinations.

A SwinTiny+FPN model (~ 33 M parameters) is trained with different subsets of the seven input channels to quantify the marginal contribution of each sensing modality (Table 5).

Table 5. Ablation study on modality combinations.

Modalities	Channels	Val mIoU	Val Dice
RGB + DEM	4	0.672	0.758
RGB + Thermal	4	0.661	0.750
RGB + DEM + Slope	5	0.721	0.798
RGB + DEM + Thermal	5	0.691	0.778
All 7 channels	7	0.743	0.821

Terrain geometry channels (DEM and Slope) contribute most to segmentation accuracy. A typical Martian landslide exhibits a steep source scarp (high slope magnitude) directly adjacent to a gently inclined depositional fan (low slope magnitude)—a morphological signature that is largely albedo-independent and therefore detectable even when the RGB channels show low contrast. Thermal inertia provides a weaker discriminative signal at its native ~ 100 m resolution, but its combination with the remaining channels reduces false positives on rocky outcrops, which share high slope values with landslide scarps but differ in thermal properties. The full 7-channel configuration achieves the highest mIoU and Dice, confirming that each sensing modality contributes independent and complementary information.

4.4.2. Ablation study on loss function

\mathcal{L}_4 (class-weighted BCE combined with soft Dice) achieves the best mIoU and the lowest fold-to-fold variance (Table 6). While Soft-IoU (\mathcal{L}_7) records a higher single-fold peak, it shows substantially greater instability across folds, a well-known characteristic of loss functions whose gradients saturate near the optimum when training sets are small [2]. Boundary Dice (\mathcal{L}_{10}) performs worst because up-weighting boundary pixels amplifies annotation noise present at the deposit perimeters in this dataset. The complementary roles of

Table 3. Progressive improvement across experimental configurations. Metrics marked (\dagger) are single-fold results on the competition validation split; all other entries are official CodaBench leaderboard scores. Configurations marked (\star) are novel architecture explorations that provide design insights but do not surpass the final UNet++ configuration on mIoU.

Configuration	mIoU	F1
SwinTiny + FPN, RGB + DEM (4 channels) \dagger	0.672	-
SwinTiny + FPN, all 7 channels \dagger	0.743	0.821
SwinTiny + FPN, class-weighted BCE + Dice \dagger	0.762	0.840
MMSFormer [17] (B2+B1 encoders), all 7 channels \dagger	0.716	-
DualSwinTiny + FPN, gated cross-modal fusion \dagger	0.793	0.848
SwinTiny + FPN (CodaBench development leaderboard)	0.837	0.884
DualSwinV2-S + UNet++, weighted-sum cross-modal fusion \dagger	0.824	0.868
DualSwinV2-S + FPN, concatenation-based cross-modal fusion \dagger	0.836	0.878
\star DualSwinV2-S + Hybrid Decoder (single-fold) \dagger	0.828	0.877
\star DualSwinV2-S + Hybrid Decoder + channel attention (5-fold CV) \dagger	0.805 ± 0.004	0.872 ± 0.004
DualSwinV2-S + UNet++, 5-fold ensemble (development)	0.867	0.905
DualSwinV2-S + UNet++, 5-fold ensemble (test)	0.783	0.800

Table 4. Online data augmentation pipeline applied during training.

Type	Transform	Setting
Geometric	Horizontal / Vertical flip	$p = 0.5$ each
	Random rotation(90°)	$p = 0.5$
	Affine transform	$\pm 5\%$ shift, $[0.9, 1.1] \times$ scale, $\pm 20^\circ$, $p=0.5$
Photometric (RGB only)	Gaussian blur	kernel 3–7, σ auto, $p=0.15$
	Brightness & Contrast	limit ± 0.2 each, $p=0.3$

Table 6. Ablation study on the loss function.

ID	Loss function	Val mIoU	Val Dice
\mathcal{L}_1	BCE	0.728	0.806
\mathcal{L}_2	Dice	0.752	0.833
\mathcal{L}_3	BCE + Dice	0.758	0.833
\mathcal{L}_4	BCE(w^+) + Dice	0.762	0.840
\mathcal{L}_5	Focal [8]	0.744	0.818
\mathcal{L}_6	Focal + Dice	0.748	0.827
\mathcal{L}_7	Soft-IoU	0.779	0.851
\mathcal{L}_8	BCE + Soft-IoU	0.751	0.827
\mathcal{L}_9	Tversky ($\alpha = 0.3$) [19]	0.747	0.827
\mathcal{L}_{10}	Dice + Boundary Dice	0.704	0.790
\mathcal{L}_{11}	Dice + Lovasz [1]	0.757	0.829
\mathcal{L}_{12}	BCE(w^+)+Dice+Lovasz	0.760	0.846

the two terms BCE providing per-pixel gradient stability and Dice providing a direct mIoU proxy justify the equal-weight combination selected for all subsequent experiments.

4.4.3. Baseline and dual-encoder

The MMSFormer baseline [17] achieves a validation mIoU of 0.716–4.6 percentage points below the SwinTiny+FPN single-encoder baseline (0.762). MMSFormer’s cross-modal transformer attention was designed and evaluated on indoor RGB-D scenes where modality co-occurrence is highly structured; its inductive biases do not transfer to planetary multi-spectral data where the seven channels arise from physically unrelated sensing phenomena. Separating feature extraction into two independent encoder streams (DualSwinTiny + FPN with gated cross-modal fusion) raises validation mIoU to 0.793, a gain of +3.1 percentage points over the single-encoder SwinTiny+FPN baseline. This confirms that modality-specific feature extraction, performed prior to any cross-modal integration, is the primary driver of Stage II improvement.

Table 7. Ablation study on the decoder choice.

Decoder	Val mIoU	Val F1
FPN [7]	0.800	0.849
UPerNet [23]	0.818	0.865
SegFormer MLP [24]	0.806	0.857
DeepLabV3+ [3]	0.801	0.846
UNet++ [26]	0.824	0.868

4.4.4. Decoder and cross-modal fusion

Two complementary ablations are conducted using the larger SwinV2-Small backbone (~ 113 M total parameters): (i) a decoder ablation with fixed weighted-sum cross-modal fusion comparing five decoder architectures (Table 7); and (ii) a fusion ablation comparing two cross-modal fusion strategies across multiple decoder choices (Table 8).

UNet++ achieves the highest mIoU in the decoder-only

Table 8. Ablation study on cross-modal fusion strategy.

Decoder	Cross-modal fusion	mIoU	F1
FPN	Concatenation-based	0.836	0.878
UPerNet	Concatenation-based	0.822	0.867
UNet++	Concatenation-based	0.814	0.857
UNet++	Weighted-sum	0.803	0.850
UPerNet	Weighted-sum	0.824	0.868

comparison owing to its dense nested skip pathways, which allow boundary-level cues at every encoder scale to propagate directly to the output without being bottlenecked by a single skip connection per resolution level. Although FPN records a marginally higher mIoU with concatenation-based fusion in Table 8, UNet++ exhibits lower fold-to-fold variance in 5-fold cross-validation, making it the more reliable choice for the final submission. Concatenation-based cross-modal fusion consistently surpasses weighted-sum fusion across all tested decoders (+0.011 mIoU on average), confirming that a learned full-rank linear interaction between RGB and auxiliary feature spaces is more expressive than a fixed scalar weighting.

4.4.5. Architecture explorations

Hybrid SegFormer-UNet++ Decoder. Analysis of per-tile predictions from the Stage III UNet++ model reveals a recurring failure mode: large, spatially diffuse landslide deposits are segmented incompletely, with isolated foreground fragments rather than continuous connected regions. This is attributed to the local nature of UNet++ skip connections, which prioritise high-frequency boundary cues over long-range scene context. A Hybrid Decoder is therefore constructed by running a UNet++ graph and a SegFormer MLP head [24] in parallel on the shared fused feature pyramid. The UNet++ path captures fine-grained boundary detail via dense skip connections, while the SegFormer path projects all four pyramid levels to a shared channel width with independent 1×1 convolutions, upsamples them to the finest scale, and aggregates them through a single 1×1 fusion, improving recall on large, diffuse deposits. The two decoder outputs are aligned to the same spatial resolution and fused by a learned 1×1 conv + BN-ReLU + SE gate before the classification head.

Table 9. Hybrid decoder vs. plain UNet++.

Decoder	mIoU	IoU _{fg}	IoU _{bg}	Prec.	Recall	F1
UNet++	0.836	0.776	0.895	0.895	0.850	0.872
Hybrid	0.828	0.769	0.887	0.856	0.899	0.877

Table 9 quantifies the precision-recall trade-off in a controlled single-fold evaluation. The Hybrid Decoder achieves

a higher F1 score (0.877 vs. 0.872) by raising recall from 0.850 to 0.899 through the SegFormer global path, at the cost of a moderate precision reduction (0.895 to 0.856) and a small mIoU penalty (0.836 to 0.828). Since mIoU is the primary MARS-LS ranking metric, plain UNet++ is used for final submission. However, when F1 or coverage recall is prioritized, the Hybrid Decoder is preferred.

Channel Attention Mechanisms. Building on the Hybrid Decoder, the effect of channel attention modules is investigated by inserting them at three positions: at the input level prior to the encoders (IA), within the encoder feature hierarchy (IE), and at the decoder output (DO). Three attention mechanisms are compared: Efficient Channel Attention (ECA) [20], Squeeze-and-Excitation (SE) [6], and Convolutional Block Attention Module (CBAM) [22]. Table 10 reports 5-fold cross-validation mIoU and F1.

All attention configurations achieve CV mIoU in the narrow range 0.802-0.806; a spread of only 0.004 points, smaller than the across-fold standard deviation of most runs. This tight clustering indicates that, given a training set of 465 tiles, the additional parameters introduced by channel attention modules do not provide a generalizable signal beyond the base concatenation-based fusion. Input-level gating (E11-E13) performs marginally worse than encoder-level gating alone (E10-a, E10-b), suggesting that applying attention prior to the dual encoders partially disrupts the modality-specific feature statistics that the dual-encoder design is intended to preserve. Channel attention is expected to provide consistent gains when the training set is substantially larger ($\gtrsim 10k$ tiles) and when modality quality varies substantially across samples.

Late Fusion Ablation. We compare our proposed mid-fusion architecture against a late-fusion variant that maintains separate encoder-decoder pipelines per modality and merges predictions via a learnable α -blend: $\hat{y} = \sigma(\alpha) \cdot L_{\text{rgb}} + (1 - \sigma(\alpha)) \cdot L_{\text{aux}}$. Despite doubling the decoder parameters, late fusion yields only a marginal mIoU difference (0.8415 ± 0.008 vs. 0.8421 ± 0.007), well within the standard-deviation overlap across 5-fold CV. Notably, the learned blending weight converges to $\alpha_{\text{rgb}} \approx 0.48$ across all folds, indicating near-equal modality reliance with a slight preference for auxiliary channels (DEM, slope), while the precision-recall trade-off shifts toward fewer false positives (+1 pp precision) at the cost of reduced recall (-0.9 pp).

4.4.6. Inference - Test-Time Augmentation Ablation

On a single model, TTA provides marginal gains or slight degradation (Table 11) depending on the transform type. Rotation-based augmentations reduce accuracy because they alter the orientation of DEM gradient and slope features; the model has been trained on orbital tiles and learns direction-sensitive filters for the typical slope of equatorial Martian terrain. Horizontal and vertical flips are approximately equivariant to the morphological landslide signature and yield

Table 10. Ablation study on channel attention. IA = input-level attention; IE = intra-encoder attention; DO = decoder-output attention.

Config.	IA	IE	DO	Attention-gated fusion	CV mIoU	CV F1
E10-a	-	ECA	-	ECA-gated	0.806 ± 0.009	0.873 ± 0.009
E10-b	-	ECA	-	CBAM-gated	0.805 ± 0.008	0.872 ± 0.009
E11	ECA	ECA	CBAM	CBAM-gated	0.802 ± 0.011	0.871 ± 0.010
E12	ECA	ECA	ECA	ECA-gated	0.805 ± 0.008	0.872 ± 0.008
E13	ECA	ECA	SE	SE-gated	0.803 ± 0.006	0.871 ± 0.007
E9	ECA	SE	CBAM	ECA-gated	0.805 ± 0.008	0.872 ± 0.008

Table 11. Ablation study on test-time augmentation.

TTA Strategy	Val mIoU	ΔmIoU	Inf. time
No TTA	0.8278	+0.0000	0.9 s
Horizontal flip	0.8272	-0.0006	1.0 s
Vertical flip	0.8276	-0.0002	1.0 s
H-flip + V-flip (2-view)	0.8283	+0.0005	1.2 s
4-view (90° rotations)	0.8271	-0.0007	1.2 s
8-view (D4 symmetry group)	0.8231	-0.0047	1.5 s

Table 12. EMA vs. standard training.

Training configuration	Val mIoU	Val F1	Best epoch
EMA ($\gamma = 0.995$)	0.8278	0.8692	28
Standard (no EMA)	0.8178	0.8611	12

marginal improvement. In the 5-fold ensemble setting, 4-view TTA is applied to reduce inter-fold prediction variance across the 20-model average, where the noise-averaging effect over independent model predictions outweighs the marginal single-model degradation.

4.4.7. Training - Exponential Moving Average Ablation

EMA yields +0.010 mIoU and shifts best checkpoint from epoch 12 to 28 (Table 12). Without EMA, validation mIoU peaks early and then fluctuates as late-stage gradient updates produce high-frequency oscillations around the loss minimum—a well-known pathology of training on small datasets. The EMA model is robust to these short-term perturbations because it tracks a long-horizon parameter average: a decay factor $\gamma = 0.995$ corresponds to an effective window of $1/(1 - \gamma) = 200$ update steps, approximately 6.7 epochs at the training batch size of 16 on 465 tiles. This allows the network to continue benefiting from informative gradient updates before the checkpoint is frozen.

5. Discussion and Future Direction

Our dual-encoder architecture preserves modality-specific inductive biases by preventing the premature merging of fundamentally different features, isolating RGB visual features from the low-level gradient statistics of DEM and Slope chan-

nels. This separation yields a +2.6% mIoU improvement over single-encoder baselines and a +4.1% gain over MMSFormer [17]. Additionally, on our limited dataset, static concat fusion avoids the overfitting inherent to ECA-gated fusion, which introduces $\sim 1M$ parameters per scale. We also identify a precision-recall tradeoff between decoder architectures. The dense nested skip connections of UNet++ propagate fine spatial details for precise boundary localization, maximizing mIoU for the MARS-LS competition. In contrast, our Hybrid SegFormer-UNet++ Decoder aggregates global context to improve the recall. This results in a superior F1 score with only a minor mIoU penalty (-0.8%), making the Hybrid model the recommended architecture for recall-critical applications like hazard inventories. Despite strong development metrics (mIoU=0.867), our model exhibits a generalization gap on the held-out test phase (mIoU=0.783, $\Delta=0.084$). Drops in both precision (0.900 \rightarrow 0.760) and recall (0.911 \rightarrow 0.860) indicate domain shift caused by target tiles originating from a different distribution. While our 5-fold ensemble and EMA weight averaging mitigate variance, the model still struggles with structural ambiguities unresolvable at a 128×128 -pixel context, including flat dust-covered albedos, zero-slope ancient landslides, and circular crater rims mimicking fresh scarps. Future work will address these spatial limitations and cross-instrument domain adaptation to align features at their native resolutions. Scaling the Hybrid Decoder to larger datasets (>10k tiles) will improve generalization without overfitting.

6. Conclusion

We presented **DualSwinFusionSeg**, a dual-encoder architecture for Martian landslide segmentation from seven-band orbital remote sensing imagery. The model processes RGB and auxiliary geophysical modalities using separate encoders, fuses the resulting multi-scale feature pyramids through lightweight concat modules, and reconstructs boundary-sensitive segmentation masks using a UNet++ decoder. Through a 13-configuration ablation study, we show that separating RGB and geophysical streams from the earliest layers substantially improves performance, providing a +2.6% mIoU gain over single-encoder fusion. We also find that simple concat-project fusion is more effective than

gated alternatives. While a Hybrid SegFormer-UNet++ decoder achieves the best F1 score by balancing precision and recall, the plain UNet++ configuration yields the highest mIoU, highlighting a trade-off between segmentation metrics. The final model achieves **0.867 mIoU** and **0.905 F1** on the PBVS 2026 MARS-LS development benchmark, and **0.783 mIoU** on the held-out test set, demonstrating the effectiveness of modality-specific encoding and lightweight multimodal fusion for planetary surface segmentation.

References

- [1] Maxim Berman, Amal Rannen Triki, and Matthew B Blaschko. The lovász-softmax loss: A tractable surrogate for the optimization of the intersection-over-union measure in neural networks. In *Proceedings of the IEEE conference on computer vision and pattern recognition*, pages 4413–4421, 2018.
- [2] Alexander Buslaev, Vladimir I Iglovikov, Eugene Khvedchenya, Alex Parinov, Mikhail Druzhinin, and Alexandr A Kalinin. Alumentations: fast and flexible image augmentations. *Information*, 11(2):125, 2020.
- [3] Liang-Chieh Chen, Yukun Zhu, George Papandreou, Florian Schroff, and Hartwig Adam. Encoder-decoder with atrous separable convolution for semantic image segmentation. In *Proceedings of the European conference on computer vision (ECCV)*, pages 801–818, 2018.
- [4] Omid Ghorbanzadeh, Yonghao Xu, Pedram Ghamisi, Michael Kopp, and David Kreil. Landslide4sense: Reference benchmark data and deep learning models for landslide detection. *arXiv preprint arXiv:2206.00515*, 2022.
- [5] Changhong Hou, Junchuan Yu, Daqing Ge, Liu Yang, Laidian Xi, Yunxuan Pang, and Yi Wen. Translandseg: a transfer learning approach for landslide semantic segmentation based on vision foundation model. *arXiv preprint arXiv:2403.10127*, 2024.
- [6] Jie Hu, Li Shen, and Gang Sun. Squeeze-and-excitation networks. In *Proceedings of the IEEE conference on computer vision and pattern recognition*, pages 7132–7141, 2018.
- [7] Tsung-Yi Lin, Piotr Dollár, Ross Girshick, Kaiming He, Bharath Hariharan, and Serge Belongie. Feature pyramid networks for object detection. In *Proceedings of the IEEE conference on computer vision and pattern recognition*, pages 2117–2125, 2017.
- [8] Tsung-Yi Lin, Priya Goyal, Ross Girshick, Kaiming He, and Piotr Dollár. Focal loss for dense object detection. In *Proceedings of the IEEE international conference on computer vision*, pages 2980–2988, 2017.
- [9] Bingxue Liu, Wei Wang, Yuming Wu, and Xing Gao. Attention swin transformer unet for landslide segmentation in remotely sensed images. *Remote Sensing*, 16(23):4464, 2024.
- [10] Ze Liu, Yutong Lin, Yue Cao, Han Hu, Yixuan Wei, Zheng Zhang, Stephen Lin, and Baining Guo. Swin transformer: Hierarchical vision transformer using shifted windows. In *Proceedings of the IEEE/CVF international conference on computer vision*, pages 10012–10022, 2021.
- [11] Ze Liu, Han Hu, Yutong Lin, Zhuliang Yao, Zhenda Xie, Yixuan Wei, Jia Ning, Yue Cao, Zheng Zhang, Li Dong, et al. Swin transformer v2: Scaling up capacity and resolution. In *Proceedings of the IEEE/CVF conference on computer vision and pattern recognition*, pages 12009–12019, 2022.
- [12] Jonathan Long, Evan Shelhamer, and Trevor Darrell. Fully convolutional networks for semantic segmentation. In *Proceedings of the IEEE conference on computer vision and pattern recognition*, pages 3431–3440, 2015.
- [13] Ilya Loshchilov and Frank Hutter. Decoupled weight decay regularization. *arXiv preprint arXiv:1711.05101*, 2017.
- [14] Sidike Paheding, Abel A Reyes, A Rajaneesh, KS Sajinkumar, and Thomas Oommen. Marsls-net: Martian landslides segmentation network and benchmark dataset. In *Proceedings of the IEEE/CVF Winter Conference on Applications of Computer Vision*, pages 8236–8245, 2024.
- [15] Sidike Paheding, Abel Reyes-Angulo, Leo Thomas Ramos, Angel D Sappa, Thomas Oommen, et al. Mmlsv2: A multimodal dataset for martian landslide detection in remote sensing imagery. *arXiv preprint arXiv:2602.08112*, 2026.
- [16] PBVS 2026 Challenge Organizers. PBVS 2026 MARS-LS: Martian landslide segmentation challenge. <https://www.codabench.org/competitions/12305/>, 2026.
- [17] Md Kaykobad Reza, Ashley Prater-Bennette, and M Salman Asif. Mmsformer: Multimodal transformer for material and semantic segmentation. *IEEE Open Journal of Signal Processing*, 5:599–610, 2024.
- [18] Olaf Ronneberger, Philipp Fischer, and Thomas Brox. U-net: Convolutional networks for biomedical image segmentation. In *International Conference on Medical image computing and computer-assisted intervention*, pages 234–241. Springer, 2015.
- [19] Seyed Sadegh Mohseni Salehi, Deniz Erdogmus, and Ali Gholipour. Tversky loss function for image segmentation using 3d fully convolutional deep networks. In *International workshop on machine learning in medical imaging*, pages 379–387. Springer, 2017.
- [20] Qilong Wang, Banggu Wu, Pengfei Zhu, Peihua Li, Wangmeng Zuo, and Qinghua Hu. Eca-net: Efficient

channel attention for deep convolutional neural networks. In *Proceedings of the IEEE/CVF conference on computer vision and pattern recognition*, pages 11534–11542, 2020.

- [21] Ross Wightman, Nathan Raw, Alexander Soare, Aman Arora, Chris Ha, Christoph Reich, Fredo Guan, Jakub Kaczmazyk, Mohammed Rizin, Hyeongchan Kim, et al. rwrightman/pytorch-image-models: v0. 8.10 dev0 release. *Zenodo*, 2023.
- [22] Sanghyun Woo, Jongchan Park, Joon-Young Lee, and In So Kweon. Cbam: Convolutional block attention module. In *Proceedings of the European conference on computer vision (ECCV)*, pages 3–19, 2018.
- [23] Tete Xiao, Yingcheng Liu, Bolei Zhou, Yuning Jiang, and Jian Sun. Unified perceptual parsing for scene understanding. In *Proceedings of the European conference on computer vision (ECCV)*, pages 418–434, 2018.
- [24] Enze Xie, Wenhai Wang, Zhiding Yu, Anima Anandkumar, Jose M Alvarez, and Ping Luo. Segformer: Simple and efficient design for semantic segmentation with transformers. *Advances in neural information processing systems*, 34:12077–12090, 2021.
- [25] Chengwei Zhao, Long Li, Yubo Wang, Xuqing Li, Chong Xu, Yubin Song, Dongsheng Ren, and Cheng Xiao. D2fls-net: Dual-stage dem-guided fusion transformer for landslide segmentation. *Plos one*, 20(11): e0337412, 2025.
- [26] Zongwei Zhou, Md Mahfuzur Rahman Siddiquee, Nima Tajbakhsh, and Jianming Liang. Unet++: A nested u-net architecture for medical image segmentation. In *International workshop on deep learning in medical image analysis*, pages 3–11. Springer, 2018.